Journal of Structural Geology 68 (2014) 82–96

Contents lists available at ScienceDirect

Journal of Structural Geology

journal homepage: www.elsevier.com/locate/jsg

Comparative mineral chemistry and textures of SAFOD fault gouge and damage-zone rocks

Diane E. Moore*

U. S. Geological Survey, 345 Middlefield Road MS/977, Menlo Park, CA 94025, USA

ARTICLE INFO

Article history:
Received 4 June 2014
Received in revised form
30 August 2014
Accepted 1 September 2014
Available online 16 September 2014

Keywords:
San Andreas Fault
SAFOD
Fault gouge
Shearing-enhanced reactions
Saponite
Corrensite

ABSTRACT

Creep in the San Andreas Fault Observatory at Depth (SAFOD) drillhole is localized to two foliated gouges, the central deforming zone (CDZ) and southwest deforming zone (SDZ). The gouges consist of porphyroclasts of serpentinite and sedimentary rock dispersed in a foliated matrix of Mg-smectite clays that formed as a result of shearing-enhanced reactions between the serpentinite and quartzofeldspathic rocks. The CDZ takes up most of the creep and exhibits differences in mineralogy and texture from the SDZ that are attributable to its higher shearing rate. In addition, a ~0.2-m-wide sector of the CDZ at its northeastern margin (NE-CDZ) is identical to the SDZ and may represent a gradient in creep rate across the CDZ. The SDZ and NE-CDZ have lower clay contents and larger porphyroclasts than most of the CDZ, and they contain veinlets and strain fringes of calcite in the gouge matrix not seen elsewhere in the CDZ. Matrix clays in the SDZ and NE-CDZ are saponite and corrensite, whereas the rest of the CDZ lacks corrensite. Saponite is younger than corrensite, reflecting clay crystallization under declining temperatures, and clays in the more actively deforming portions of the CDZ have better equilibrated to the lower-temperature conditions.

Published by Elsevier Ltd.

1. Introduction

The San Andreas Fault Observatory at Depth (SAFOD) has provided the unparalleled opportunity to examine core samples from an active plate-boundary fault at depth. In 2004 and 2005, the main hole was drilled across the San Andreas fault (SAF) in the central creeping section NW of Parkfield (Fig. 1A and B), where the creep rate is ~25 mm/yr (Titus et al., 2006). Coring operations in 2007 focused on two positions of well-casing deformation attributed to creep that were identified at true vertical depths of ~2.65 and ~2.7 km and temperatures of 112–114 °C; both zones were successfully sampled during coring (Fig. 1C and D). The 2.6-m-wide central deforming zone (CDZ) (Zoback et al., 2010, 2011) is situated near the middle of the 200-m-wide damage zone of the currently active fault, and it accommodates most of the slip. The less active, 1.6-m-wide southwest deforming zone (SDZ) marks the SW limit of the SAF damage zone (Zoback et al., 2010, 2011). Variably deformed shales, siltstones, and fine-grained sandstones adjoin both gouge zones (Fig. 1E) (Bradbury et al., 2011; Holdsworth et al., 2011). The damage zone of the presently active trace at SAFOD lies completely within North American plate rocks (Fig. 1C) (Zoback et al., 2010, 2011).

The two creeping traces share many similarities and they differ markedly in texture, chemistry, and mineralogy from the adjoining wall rocks. Whole-rock X-ray fluorescence (XRF) compositions of the CDZ and SDZ (Bradbury et al., 2011; Janssen et al., 2014) are depleted in Si and very enriched in Mg and the trace elements Cr and Ni compared to the quartzofeldspathic damage-zone rocks, consistent with a large ultramafic component to the creeping traces. The CDZ and SDZ consist of porphyroclasts of serpentinite and a variety of other, largely sedimentary rock types dispersed in a foliated matrix of Mg-rich clays. Serpentine is not present elsewhere in the core (Holdsworth et al., 2011; Kienast et al., 2012; Moore and Rymer, 2012). The porphyroclasts within the CDZ and SDZ show a strong preferred orientation subparallel to the plane of the SAF, indicating distributed shear across the gouge zones (Chester et al., 2010; Sills, 2010). The general lack of cementation or of cross-cutting veins in the gouge matrix also is consistent with distributed shear (e.g., Holdsworth et al., 2011; Hadizadeh et al., 2012; Moore and Rymer, 2012).

A tectonic sliver of serpentinite extends for at least several kilometers along strike in the surface trace of the San Andreas fault near the drillsite (Moore and Rymer, 2012). The same Mg-clay-rich gouge as found in the SAFOD core was identified along the faulted

* Tel.: +1 (650) 329 4825.
E-mail address: dmoore@usgs.gov.

http://dx.doi.org/10.1016/j.jsg.2014.09.002
0191-8141/Published by Elsevier Ltd.

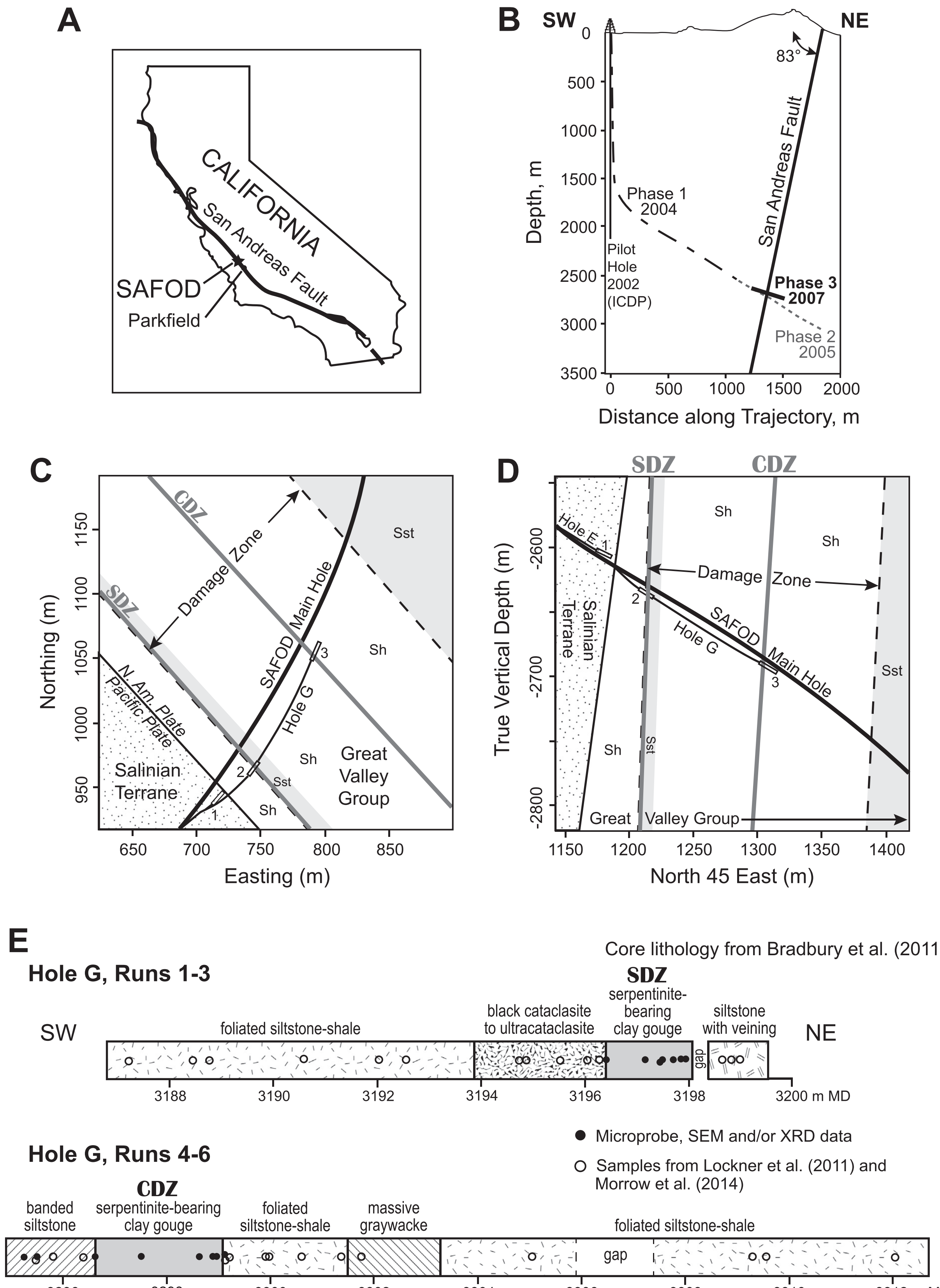

Fig. 1. A) Location and B) summary of drilling operations at SAFOD. C) Map and D) cross-sectional views of the SAFOD main borehole and Phase 3 sidetrack boreholes (Holes E and G) relative to the SAF at a depth of ~2.7 km (figures modified from Phase 3 Core Atlas and Zoback et al., 2011). Dashed lines mark the limits of the SAF damage zone, defined by low seismic velocities, which lies within North American Plate rocks of the Great Valley Group. The positions of the two creeping traces, the CDZ and SDZ, are indicated by dark-gray lines. The CDZ is located in the center and the SDZ at the SW margin of the damage zone. Numbered boxes show the positions of the recovered Phase 3 core samples. E) Samples featured in this study (filled circles) in the Hole G core, plotted on the lithologic sections of Bradbury et al. (2011). Open circles are samples examined by the author (XRD, thin sections) for the laboratory studies of Lockner et al. (2011) and Morrow et al. (2014).

Table 1
SAFOD core samples described in this study.

Depth (m MD)	Depth (ft)	Core box position	Lithology
3196.38	10486.8	G-2-7 6–11.5 cm	Cataclasite/SDZ boundary
3197.24	10489.6	G-2-8 0–7 cm	SDZ
3197.70[a]	10491.1	G-2-8 45–50 cm	SDZ
3197.71	10491.2	G-2-8 50–55 cm	SDZ
3197.82	10491.5	G-2-9 5–10 cm	SDZ[b]
3197.88	10491.7	G-2-9 10–14 cm	SDZ[b]
3197.91	10491.8	G-2-9 14–16 cm	SDZ[b]
3295.25	10811.2	G-4-1 34–37 cm	Banded siltstone
3295.53	10812.1	G-4-1 60–64 cm	Banded siltstone
3296.60[a]	10815.6	G-4-2 75–81 cm	Siltstone/CDZ boundary
3297.55[a]	10818.7	G-4-3 84–85 cm	CDZ
3298.63[a]	10822.3	G-4-5 14–20 cm	CDZ
3298.89	10823.1	G-4-5 41–44 cm	CDZ
3298.92	10823.2	G-4-5 44–48 cm	CDZ
3299.10	10823.9	G-4-5 64–67 cm	Foliated siltstone

[a] Studied previously by Moore and Rymer (2012).
[b] Includes portions of the 9-cm serpentinite porphyroclast.

contact of the serpentinite against a Tertiary sandstone/siltstone. Moore and Rymer (2012) concluded that the surface exposures of serpentinite and gouge connect to the CDZ and SDZ at depth, and that the serpentinite had been tectonically entrained into the SAF from a deep source identified on the NE side of the fault from aeromagnetic surveys (McPhee et al., 2004). The Mg-rich clayey gouge was interpreted to be the product of shearing-enhanced metasomatic reaction of the serpentinized ultramafic rock with the quartzofeldspathic crustal wall rocks of contrasting chemistry (Moore and Rymer, 2012; Bradbury et al., 2013). Moore and Lockner (2013) duplicated this reaction in laboratory friction experiments at hydrothermal conditions that also were characterized by the rapid onset of weakening and stabilization of slip (creep). Based on the timing of major changes in the regional deformation patterns, Titus et al. (2011) concluded that the tectonic incorporation of serpentinite into the fault zone and the onset of creep in the central creeping section of the SAF took place 2–2.5 m.y. ago.

Recently acquired Phase 3 core samples allow further comparison of the CDZ and SDZ not only with the sedimentary/metasedimentary wall rocks but also with each other. The goals of this paper are: (1) to illustrate the abrupt changes in texture, mineralogy, and chemistry that occur across the boundaries of the CDZ and SDZ with the quartzofeldspathic rocks; (2) to document the migration of Mg-bearing fluids for short distances into the wall rocks from the creeping traces; and (3) to highlight some differences in mineral chemistry and, to a lesser extent, texture between the CDZ and SDZ and also across the width of the CDZ that may be attributable to differences in shearing rate.

2. Samples studied and methods

Core samples featured in this study (photomicrographs, X-ray diffraction (XRD) and/or microprobe data) are listed in Table 1, and their positions in the core are marked by filled circles on the lithologic sections of Bradbury et al. (2011) in Fig. 1E. Reported depths are the measured depths in Hole G determined during Phase 3 core recovery and utilized in the Phase 3 Core Atlas (http://www.earthscope.org). The focus of this work is on samples that span the widths of the CDZ and SDZ and the wall rocks immediately adjacent to them. In addition, thin-section and XRD examination of samples used by Lockner et al. (2011) and Morrow et al. (2014) for laboratory friction and permeability tests, respectively (open circles in Fig. 1E), has provided a valuable overview of the rock units in Hole G, although those data are incorporated to only a minor degree in this paper. The samples are not oriented, although in most cases the upward direction of the core in the borehole is known.

This study is based largely on examination of polished thin sections. Because of the fine-grained nature of many of the samples, much of the petrographic work was conducted using a scanning electron microscope (SEM) equipped with an energy dispersive spectrometer (EDS). The EDS capability aided in mineral identifications and provided qualitative information on mineral chemistry. Mineral identifications were augmented by XRD analyses of packed-powder, bulk-rock samples run at 1° 2θ per minute scanning rate and 0.01° sampling width; all of the samples marked in Fig. 1E were tested in this manner. Selected X-rayed samples were held in an ethylene glycol atmosphere for 3 days, then reanalyzed for identification of swelling clays (Reynolds, 1988; Moore and Reynolds, 1997). Two samples straddle the southwest boundaries of the CDZ and SDZ with adjoining rock units, and element maps across the boundaries were acquired with an electron probe microanalyzer (EPMA). The pixel size was 1 μm × 1 μm, and the image size was a square 1024 pixels on a side. Scans were obtained along a linear traverse at 1 mm spacings, to allow for some overlap between adjacent images. Data collection for each image lasted ~3.5 h; all of the scans for a given element were adjusted to encompass the same intensity range.

Quantitative chemical analyses of a variety of Mg-rich phyllosilicates were made using EPMA at conditions of 15 kV accelerating voltage, 10 nA beam current, and 5 μm beam diameter. The procedures are the same as outlined by Moore and Rymer (2012). The 5-μm spot diameter that was adopted after several trials is larger than the grain size of many of the analyzed phyllosilicate minerals. Because of this, a given spot analysis might represent, in some cases, a polycrystalline aggregate of a single mineral that likely includes some pore space, thus lowering the anhydrous total. The typically poor polish of thin sections containing clays can also yield low anhydrous totals. Alternatively, a given composition could represent domains of different phyllosilicate minerals within a larger, composite crystal or a physical mixture of one or more phyllosilicates with traces of other minerals such as calcite, quartz, or feldspar. More than half the data collected from the samples of gouge matrix were discarded because of low totals, obvious contamination, or unreasonable calculated structural formulas.

3. Effects of drilling mud and cutting fluids

To minimize contamination by clays during Phase 3 core recovery, instead of bentonite the drilling “mud” consisted of a rock flour augmented with barite in a concentrated $CaCl_2$ solution. A similar brine was subsequently used for processing core at the repository. The poorly consolidated fault gouge shows some evidence of contamination by the drilling mud and possibly the processing fluids. The effects are particularly marked at the two gouge-wall rock boundaries examined in this study, perhaps because of the abrupt changes in mechanical strength across the contacts (Lockner et al., 2011; Carpenter et al., 2012). A wedge of drilling mud was injected along the contact between the cataclasite and the SDZ (Fig. 2A). As viewed in this thin section, the wedge is 3 mm wide at the perimeter of the core, but tapers down to ≤0.2 mm at distances >10 mm from the edge. A finer-grained fraction of the rock flour was injected farther into the cored cylinder than the coarser-grained material that is concentrated near the perimeter. The bright flecks in the drilling mud (Fig. 2A) are the barite, a common additive used to increase the density of the mud. The composition of the drilling-mud barite generally is near the barium end member, ($BaSO_4$ (Supplementary Fig. 1A). On the other hand, natural barites in the SAFOD core commonly contain moderate to

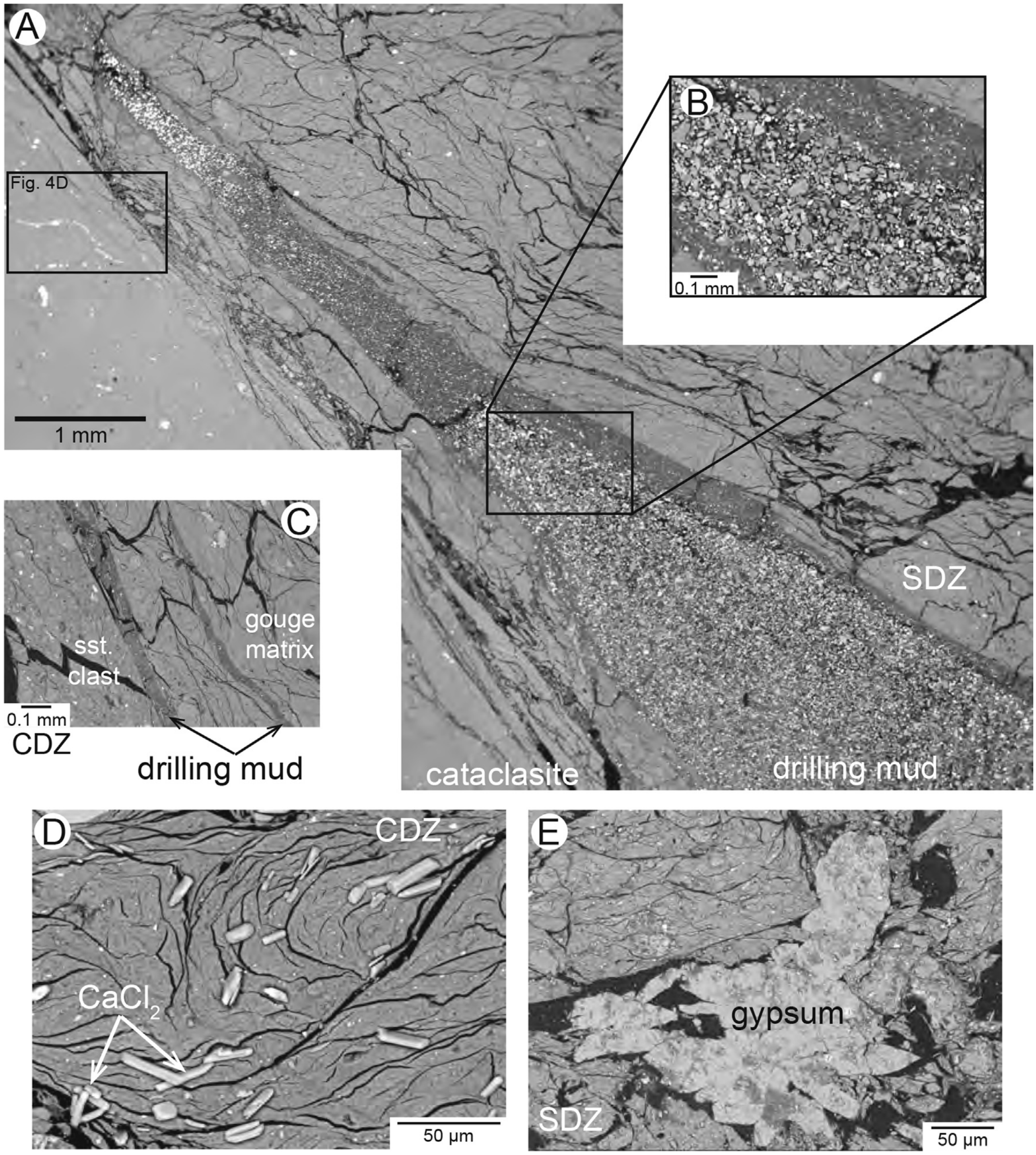

Fig. 2. Contamination of core resulting from coring and processing procedures; all photos are backscattered-electron (BSE) scanning electron microscope (SEM) images. A–B) A wedge of the rock flour used as drilling mud was injected along the contact between cataclasite and the SDZ (3196.38 m). Bright flecks are barite. C) Narrow bands of fine-grained drilling mud fill partings along the foliation in the CDZ gouge (3298.92 m). At left is a porphyroclast of siltstone (sst). D) Rods of $CaCl_2$ have precipitated near the perimeter of the CDZ core (3296.60 m). E) Clusters of calcium sulfate, probably gypsum, fill a disturbed spot in a sample of the SDZ gouge (3196.38 m).

substantial amounts of the Sr end-member, celestine ($SrSO_4$; Supplementary Fig. 1B), and some crystals may be better termed celestine than barite. The barite compositions help to distinguish between drilling mud and fault gouge that was disrupted but not otherwise contaminated during coring or processing. The southwest boundary of the CDZ with the banded siltstone also is marked by drilling mud. The siltstone is more highly fractured than the cataclasite adjoining the SDZ, and a mixture of drilling mud with fragments of gouge and siltstone was injected into a few of those fractures rather than along the boundary (Fig. 3A).

The fine fraction of the drilling mud also was injected into the CDZ and SDZ along foliation surfaces (Fig. 2C). In addition, crystals of $CaCl_2$ (Fig. 2D) and calcium sulfate (Fig. 2E), probably gypsum ($CaSO_4 \cdot 2H_2O$), along with some cubes of NaCl, have precipitated in the gouges from the drilling and/or processing fluids. These deposits are more abundant near the perimeter of the core. No evidence of contamination from either the drilling mud or the processing fluids has as yet been found in the wall rocks at distances greater than a few mm from the CDZ and SDZ.

It is possible that the Ca-rich drilling fluids and the processing fluids have affected the exchangable cation contents of the swelling clays, given that the dominant interlayer cation in the clays is Ca (Table 2). However, the clays also contain moderate amounts of Na and minor K, and the relative abundances of Ca, Na, and K in the clay minerals reflect the whole-rock CDZ and SDZ compositions reported by Bradbury et al. (2011). In any case, it is the total interlayer charge, not the identity of the exchangable cations (whether Ca, Na, or K), that is of most importance to this study.

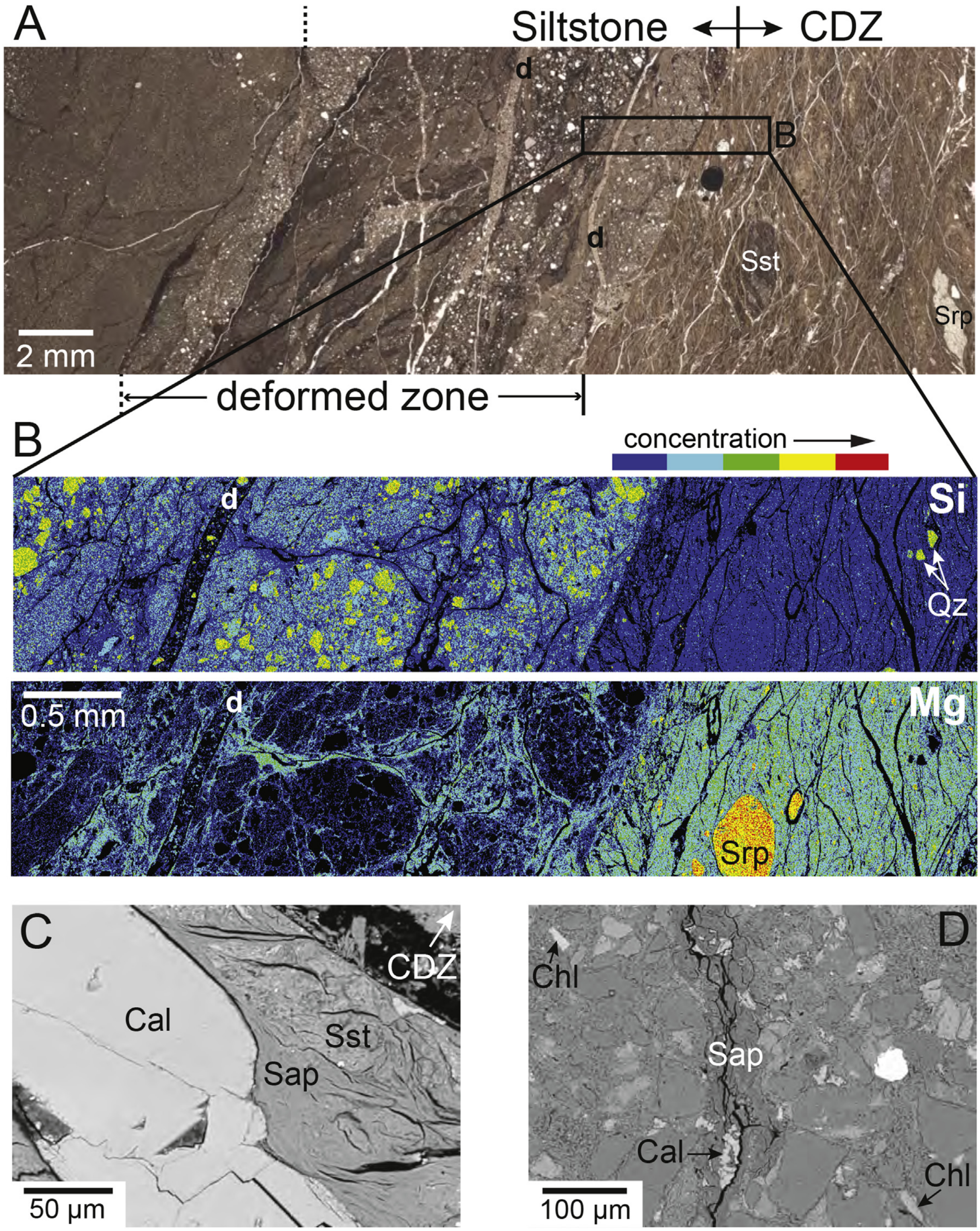

Fig. 3. Southwest boundary of the CDZ with the banded siltstone (3296.6 m). A) Portion of a thin section scan that shows a ~10 mm wide band of deformed siltstone adjacent to the boundary. Dashed lines mark the transition from deformed to undeformed siltstone. The black rectangle indicates the extent of the element maps in B). B) Contrast in Si and Mg concentrations of the CDZ and siltstone on either side of the contact. Narrow bands of relatively high Mg and low Si content in the siltstone are fractures filled with Mg-rich saponitic clays. Abbreviations: d, fractures that contain drilling mud; Qz, quartz; Srp, serpentinite; Sst, siltstone. C–D) BSE images from the same thin section as A–B), but rotated ~90° relative to them. C) Deposit of calcite (Cal) + saponite (Sap) in altered siltstone at the contact with the CDZ. D) Saponite and calcite lining an irregular crack through essentially undeformed siltstone ~9 mm from the contact with the CDZ. The crack, which is oriented at an angle of ~50° to the CDZ boundary in the thin section, terminates 1.5 mm further from the boundary. Relatively Fe-rich chlorite (Chl) is part of the siltstone mineral assemblage.

4. Petrography and XRD

Petrographic observations, augmented by XRD to verify clay–mineral identities, focused on three topics: a) the nature of contacts of the CDZ and SDZ with adjoining rock units; b) the occurrence of other Mg-rich phyllosilicate minerals in the wall rocks; and c) comparison of the textures and clay mineralogy of the CDZ with those of the SDZ.

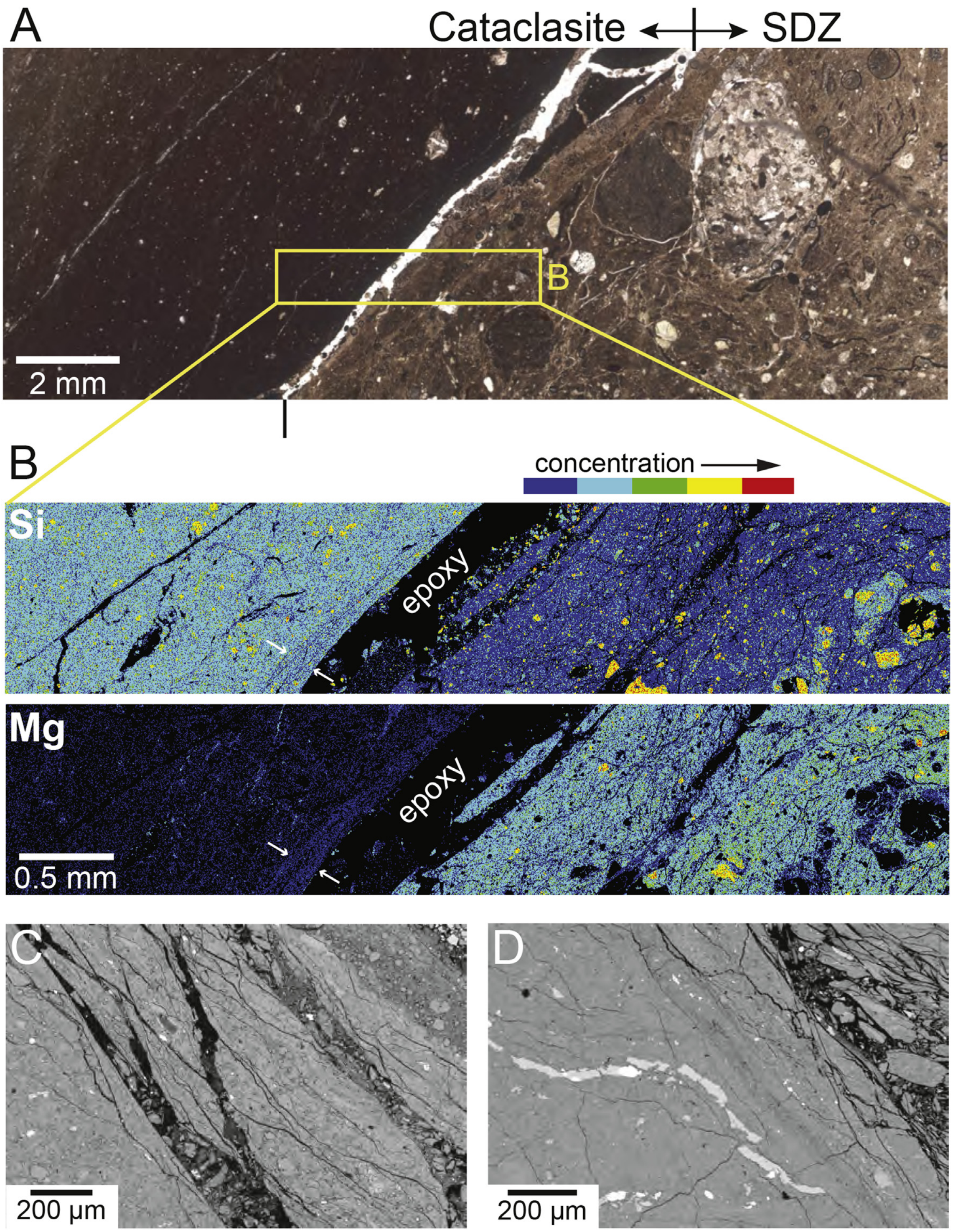

Fig. 4. Southwest boundary of the SDZ with the cataclasite (3196.38 m). A) Portion of a thin section scan showing the boundary in an area relatively free of drilling mud. The yellow rectangle outlines the extent of the element maps in B). B) Element maps of Si and Mg across the cataclasite-SDZ contact. Concentrations of both elements change abruptly at the contact, although a ≤0.3 mm wide band of the cataclasite immediately adjacent to the contact (delimited by pairs of white arrows) is very slightly enriched in Mg and depleted in Si compared to the rock farther from the SDZ. C–D) Bands of fractured, foliated, and ground-up cataclasite localized within ~1 mm of the SDZ. Dark (epoxy), fragmented areas are places where the core was disturbed during drilling. Both are BSE images from the same thin section as A–B), but rotated ~90° relative to them; D) is a close-up of part of Fig. 2A.

4.1. Gouge–wall rock boundaries

Thin sections of the southwest boundaries of the CDZ (Fig. 3) and SDZ (Fig. 4) illustrate the marked contrasts in texture, rock chemistry, and mineralogy across the contacts. The banded siltstone on the SW side of the CDZ consists of alternating sandy, silty, and shaly layers (Bradbury et al., 2011; Holdsworth et al., 2011), and a band of siltstone ~10 mm wide has been smeared out along the contact, facilitated by deformation of thin shaly layers (Fig. 3A). At distances greater than ~10 mm from the contact,

Table 2
Representative compositions of Mg-phyllosilicates in SAFOD core.[a]

	Serpentine	Saponite[b]		Corrensite[b]		Corrensite-chlorite	Chlorite
	CDZ 3297.55 m	CDZ 3297.55 m	SDZ 3197.70 m	CDZ 3298.92 m	SDZ 3197.91 m	Siltstone 3295.52 m	SDZ 3197.70 m
SiO_2	39.66	47.75	46.51	37.77	38.32	34.80	30.62
TiO_2		0.02	0.04	0.27	0.13	0.03	
Al_2O_3	1.21	5.07	5.49	10.49	11.12	15.68	19.73
Cr_2O_3	0.64	0.07	0.01	0.13	0.09	0.03	0.01
FeO	4.85	4.80	5.02	7.23	8.39	8.14	5.49
NiO	0.05	0.14	0.10	0.31	0.21	0.16	0.21
MnO	0.09	0.08	0.10	0.16	0.16	0.07	0.07
MgO	36.07	23.83	22.58	24.54	23.03	24.23	28.90
CaO	0.18	1.91	2.14	1.88	0.99	0.76	0.23
Na_2O	0.01	0.80	0.83	0.37	0.54	0.28	0.03
K_2O		0.09	0.15	0.09	0.26	0.05	0.01
Total	82.76	84.56	82.97	83.24	83.24	84.23	85.30
Si	3.96	3.57	3.55	6.75	6.84	6.15	5.94
Al^{IV}	0.04	0.43	0.45	1.25	1.16	1.85	2.06
Al^{VI}	0.10	0.02	0.05	0.96	1.18	1.42	2.46
Ti				0.03	0.02		
Cr	0.05			0.02	0.02		
Fe	0.40	0.30	0.32	1.07	1.25	1.20	0.88
Ni		0.01	0.01	0.05	0.05	0.02	0.04
Mn	0.01	0.01	0.01	0.02	0.02	0.01	0.02
Mg	5.36	2.65	2.57	6.52	6.11	6.37	8.36
Ca	0.02	0.15	0.18	0.36	0.19	0.14	0.04
Na		0.12	0.12	0.13	0.18	0.10	
K		0.01	0.01	0.02	0.06	0.01	
O	14	11	11	25	25	25	28

[a] All compositional data used in this paper are reported in Supplementary Tables 1–6.
[b] See text for an explanation of the mineral identifications.

however, the siltstone appears to be undeformed (Fig. 3A) and shows good preservation of bedding features (e.g., Holdsworth et al., 2011; Morrow et al., 2014). The foliation in the narrow deformed zone of siltstone is an older deformation feature that has been overprinted by dilational fractures. Element maps that traverse the SW margin of the CDZ (Fig. 3B) illustrate the marked chemical contrast between the gouge and the adjacent, quartzofeldspathic crustal rocks. Overall, the CDZ is characterized by lower Si and significantly higher Mg contents than the siltstone. However, fractures that crosscut the foliation have Mg and Si concentrations similar to those in the CDZ. Fluids from the CDZ have migrated into the siltstone along the fractures, depositing Mg-rich smectitic clays ± calcite (Fig. 3C and D; see also Fig. 4G of Moore and Rymer, 2012). Based on EDS measurements these clays have similar composition to those in the nearby gouge. The number of Mg-clay-lined fractures decreases with increasing distance from the boundary; only a few can be traced more than 20 mm from the contact. None of the other examined samples of the banded siltstone (Fig. 1E) contain Mg-clay-lined fractures. A few dilational fractures filled with Mg-rich clays also are present in the siltstone-shale bounding the CDZ on the NE side (3299.13 m), but the amount of fluid infiltration from the CDZ at this location seems lower than on the SW side.

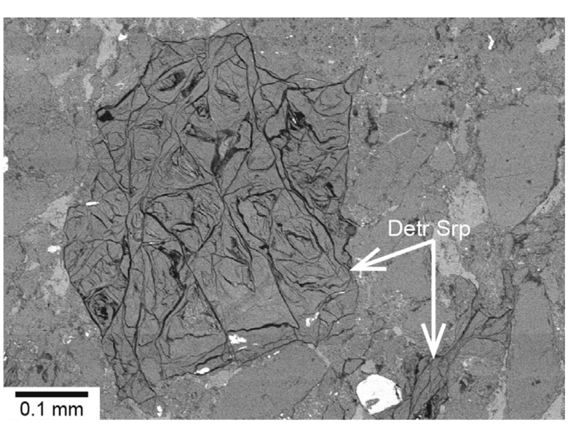

Fig. 5. Detrital serpentine grains (3295.53 m) in the banded siltstone on the SW side of the CDZ (BSE image). The larger grain consists of mesh-texture serpentine; the smaller grain at lower right has been smeared out between harder clasts. The serpentine minerals have been pseudomorphically replaced by Mg–Al-rich clays.

Rock units located SW of the SDZ have been variably deformed, and they were regarded as an older, inactive fault by Holdsworth et al. (2011). Sills (2010) determined that only those microscopic foliation planes in the cataclasite closest to the SDZ are oriented consistent with the present-day stress state of the SAF; the rest are oblique. The cataclasite immediately adjacent to the SDZ (Fig. 4A and B) is a dense, fine-grained, quartz-rich rock, and recent deformation is limited to a band of fragmented, somewhat foliated rock <2 mm in width along the contact (Figs. 2A and 4C and D). A very slight reduction in Si and enrichment in Mg occurs in a ~200 μm-wide band of the cataclasite at the contact (Fig. 4B), and SEM examination shows trace amounts of Mg-smectite clays in that band. A cataclasite sample located ~0.1 m from the SDZ (3196.28 m; Morrow et al., 2014) contains two narrow microfractures filled with clays enriched in Mg compared to those elsewhere in the rocks SW of the SDZ (e.g., Holdsworth et al., 2011; Schleicher et al., 2012). The NE boundary of the SDZ was not recovered during coring (Fig. 1E), and none of the examined core samples from the siltstone on the NE side shows evidence of infiltration of Mg-bearing fluids from the SDZ.

4.2. Other Mg-rich phyllosilicates in wall rocks

Outside of the SDZ, no traces of serpentine have been identified in any of the examined core samples from Hole G, Runs 1–3

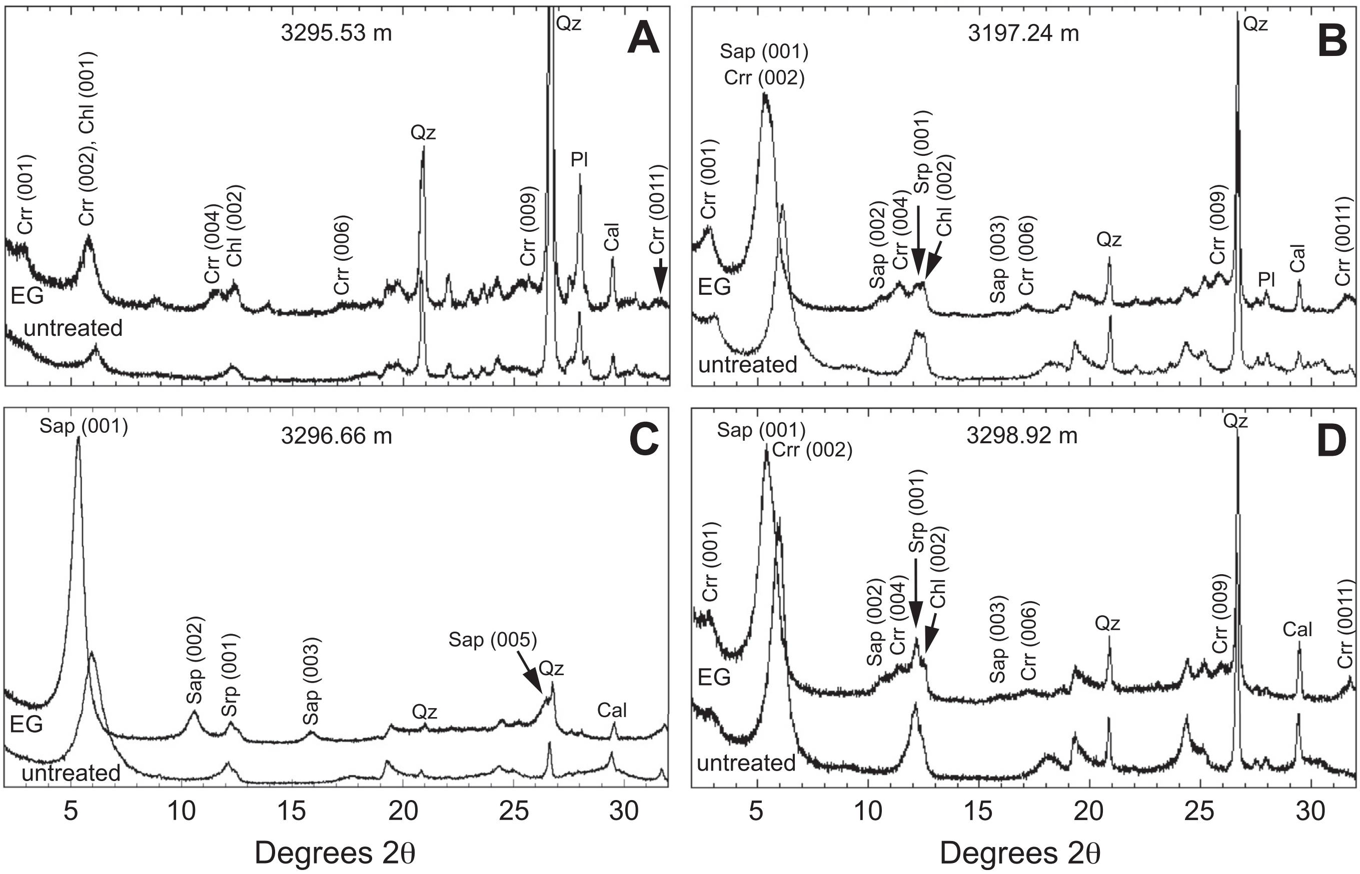

Fig. 6. Rock-powder X-ray diffraction patterns (Cu K-alpha) of untreated and glycolated (EG) samples from A) banded siltstone, 3295.53 m; B) SDZ, 3197.24 m; C) CDZ, 3296.66 m; and D) CDZ, 3298.92 m. Abbreviations: Crr, corrensite; Ilt, illite; Pl, plagioclase.

(Fig. 1E). No serpentine minerals are now present on either side of the CDZ, either, consistent with the observations of Solum et al. (2006), Holdsworth et al. (2011), and Kienast et al. (2012). However, the sedimentary wall rocks of Hole G Runs 4–6 did contain varying amounts of detrital serpentine grains that occur as irregularly shaped flakes, many of which are flattened parallel to the bedding or deformed between stronger grains (Fig. 5). The internal textures are characteristic of serpentinite, some of them showing recognizable mesh and/or bastite texture, others having a sheared appearance. Nearly all the detrital serpentine occurs in the banded siltstone on the southwest side of the CDZ, and the approximate modal percentages range between 0 and ~13% (Supplementary Fig. 2). The single, moderately high-Mg whole-rock composition (~10.5 wt% MgO) outside the foliated gouges reported by Bradbury et al. (2011) was from this banded siltstone, at ~3295.8 m. Only four of the examined samples from the rock units NE of the CD (open circles in Fig. 1E) show any evidence of detrital serpentine, and the maximum modal abundance is 0.3%.

The serpentine minerals in the detrital grains have been thoroughly replaced by Mg-rich phyllosilicates whose EDS spectra contain substantially larger Al and smaller Si and Mg peaks than are characteristic of serpentine, and somewhat larger Al and smaller Si peaks than the clays of the CDZ and SDZ. The siltstone sample containing ~13% detrital serpentine (3295.53 m) shows the presence of corrensite and chlorite in XRD patterns (Fig. 6A).

4.3. Comparison of CDZ and SDZ

Although the CDZ and SDZ share a common origin and are very similar overall, all but a 0.2-m-wide section of the CDZ at its NE end (NE-CDZ) is distinguishable from the SDZ in terms of mineralogy and, to a lesser extent, texture. The northeast margin of the CDZ is highlighted in the Phase 3 Core Atlas as a zone rich in serpentinite and sandstone blocks (shown in Supplementary Fig. 3). As many porphyroclasts ≥2 cm in length are visible on the perimeter of the core in this narrow zone as can be seen across the rest of the CDZ (Phase 3 Core Atlas). The NE-CDZ also contains a higher concentration of small (<2 cm) porphyroclasts than the rest of the CDZ (Figs. 3A and 7). The largest porphyroclasts in the creeping traces are ~40 and ~9 cm-diameter serpentinite porphyroclasts (Phase 3 Core Atlas; Fig. 7A of Bradbury et al., 2011), which together comprise ~25 volume percent of the recovered SDZ core. Quantitative porphyroclast abundances and size distributions across the widths of the CDZ and SDZ have not as yet been determined.

All of the SDZ samples examined in this and previous studies (Lockner et al., 2011; Moore and Rymer, 2012; Morrow et al., 2014) contain both saponite and corrensite, as determined by XRD analysis (Fig. 6B). Corrensite is readily identified in the untreated powder diffraction patterns by the (001) peak at 29–30Å, representing the ordered, 1:1 alternation of saponite and chlorite layers that defines the crystal structure. In untreated samples, the saponite (002) peak at ~12° 2θ is very weak, and the corrensite (004) peak overlaps the serpentine (001) and chlorite (002) peaks. In glycolated samples, both saponite (002) and corrensite (004) peaks are resolved at ~10.5° and 11.5° 2θ, respectively (Fig. 6B). In addition, a relatively diffuse peak at ~18° 2θ in the untreated sample is replaced by a corrensite (006) peak at ~17° 2θ and a minor saponite (003) peak at ~16° 2θ in the glycolated sample. Saponite without associated corrensite is present in nearly all of the CDZ samples

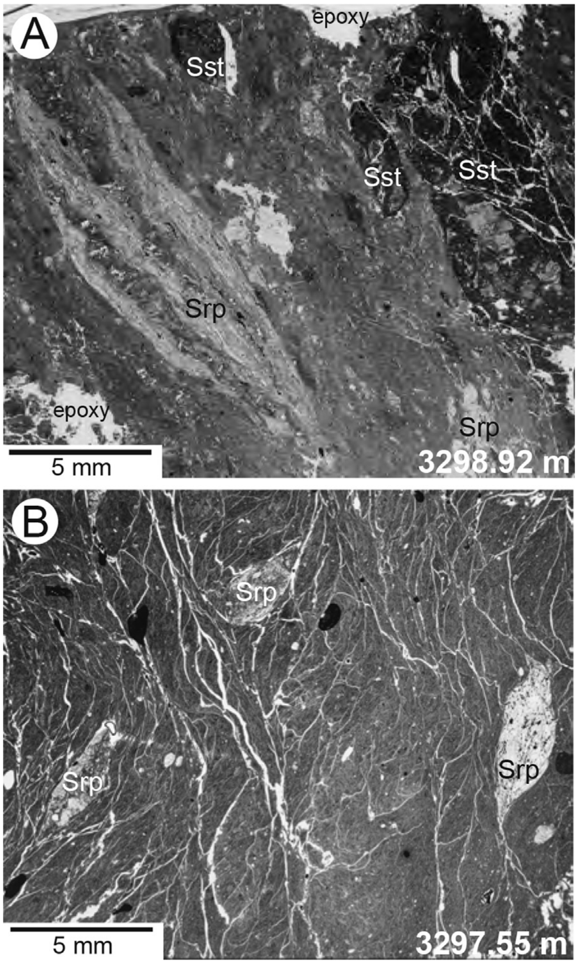

Fig. 7. Gouge textures in different parts of the CDZ (thin section scans). A) Porphyroclast-rich CDZ gouge near its NE boundary, 3298.92 m. The siltstone porphyroclasts at upper right are derived from the foliated siltstone-shale unit adjacent to the CDZ on the NE side. B) Clay-matrix-rich gouge near the middle of the CDZ (3297.55 m).

(Fig. 6C); only the narrow zone at the NE boundary contains both corrensite and saponite (Fig. 6D).

Comparison of peak heights at ~6° (saponite (001) ± corrensite (002)) and 26.65° (quartz (101), serving as a qualitative indicator of sedimentary porphyroclast abundance) suggests the dominance of Mg clays across much of the CDZ (Fig. 6C, Supplementary Fig. 4). However, substantial amounts of quartz are present in the NE-CDZ and the SDZ samples (Fig. 6B and D; Supplementary Figs. 4 and 5).

With respect to gouge textures, Moore and Rymer (2012) described the occurrence of calcite veinlets in the matrix of the SDZ; Fig. 8A shows a vein of calcite with minor barite that is nearly 6 mm in length. The calcite in this occurrence has a blocky appearance and is reasonably free of twins. Fig. 8B shows a very contorted calcite veinlet in a lozenge of the clay-rich matrix in the SDZ; most of the calcite in this deposit is highly twinned. Occurrences such as the one in Fig. 8B may represent somewhat older calcite veins that have subsequently been deformed by shear. Similar calcite veins have not yet been found across most of the width of the CDZ, but the NE margin of the CDZ contains numerous calcite veinlets along slip surfaces (Fig. 8C) and strain fringes (Passchier and Trouw, 2005) at the edges of porphyroclasts (Fig. 8D). No calcite veins cross-cutting the foliation have been seen in either the SDZ or CDZ.

5. Mineral chemistry

Selected compositions of serpentine and of trioctahedral phyllosilicate minerals in the series saponite–corrensite–chlorite are listed in Table 2, with total Fe contents reported as ferrous. Additional data for serpentine are presented in Supplementary Table 1. All of the data plotted in Figs. 9 and 10 are contained in Supplementary Tables 2–6. The occurrence (e.g., matrix clay, vein filling) of each analysis is specified in notes accompanying the supplementary tables.

5.1. Serpentine

No completely fresh serpentine analyses were obtained from either the CDZ or SDZ. Only 3 out of >120 spot analyses contained <0.2 wt% ($CaO + Na_2O + K_2O$), and most contained >0.5 wt% (Table 2; Supplementary Table 1). The presence of Ca, Na, and K, which do not fit into the serpentine structure, is an indicator of incipient replacement by smectitic clays. Most of the serpentine minerals also are depleted in Mg relative to Si, and the calculated structural formula typically has Si > 4 ($O_{anhydrous} = 14$). The low Mg contents are also attributed to partial replacement by clay minerals. The ratio Mg/(Mg + Fe) for the least altered serpentine ranges from 0.86 to 0.96.

5.2. Mg-rich smectite clays

Mineral chemical data for Mg clays from within and adjacent to the CDZ and from the SDZ are compared in Fig. 9, in plots of the atomic ratios $Si/(Si + Al_{tot})$ and Mg/(Mg + Fe). An attempt was made to obtain compositions of the fracture-filling Mg-rich smectite clays in the wall rocks on both sides of the CDZ and SDZ. To date, only those occurrences adjacent to the SW margin of the CDZ (e.g., Fig. 3C) have yielded good-quality compositions; these are plotted in Fig. 9A. The clays have a restricted compositional range, with ~5–7 wt% Al_2O_3, 22–24 wt% MgO, and ~4–5 wt% FeO (Supplementary Table 2). The ratio Mg/(Mg + Fe) varies between 0.89 and 0.91 (Fig. 9A), within the 0.86–0.96 range of serpentine. The ratio Si/(Si + Al) also is very closely constrained between 0.85 and 0.89. The structural formula averaged from the data in Supplementary Table 2 is consistent with saponite: $(0.5Ca,Na)_{0.4}(Fe,Mg)_{2.95}Al_{0.05}(Si_{3.55},Al_{0.45})O_{10}(OH)_2 \cdot nH_2O$. The minor octahedral Al content may indicate a small percentage of chlorite interlayers.

The analyzed CDZ samples are plotted in Fig. 9B–E, progressing from SW to NE, and the corresponding compositional data are presented in Supplementary Table 3. The Mg clays located ≤30 mm from the SW boundary (Fig. 9B) have essentially the same compositions as those on the other side (Fig. 9A), although the Mg/(Mg + Fe) ratio in the CDZ clays is shifted to a slightly lower range of 0.86–0.90. The data in Fig. 9B define a roughly linear trend, with the proportions of Mg and Si varying directly. Clays from the sample located near the center of the CDZ (3297.55 m, Fig. 9C) are identical in composition to those on the SW side (Fig. 9B). The sample at 3298.63 m is located about 0.2 m from the edge of the clast-rich zone (Supplementary Fig. 3), and clay compositions are shifted to slightly lower Si ratios between 0.79 and 0.86. The data in Fig. 9E are from the clast-rich portion of the CDZ that contains both corrensite and saponite (Fig. 6D), and the compositional range has expanded to Mg/(Mg + Fe) ratios as low as 0.81 and Si/(Si + Al) down to 0.75. Several of the clays with compositions similar to the saponites in Fig. 9A fill fractures in porphyroclasts or are associated with calcite deposits in the gouge matrix on the NE side (Fig. 8C and D).

The analyzed SDZ samples consist of: 1) the sample at the SW boundary, 3196.38 m (Fig. 9F); 2) one at 3197.70 m (Fig. 9G); and 3) a group of three samples on either side of the 9-cm serpentinite porphyroclast located near the NE boundary (3197.82–3197.91 m;

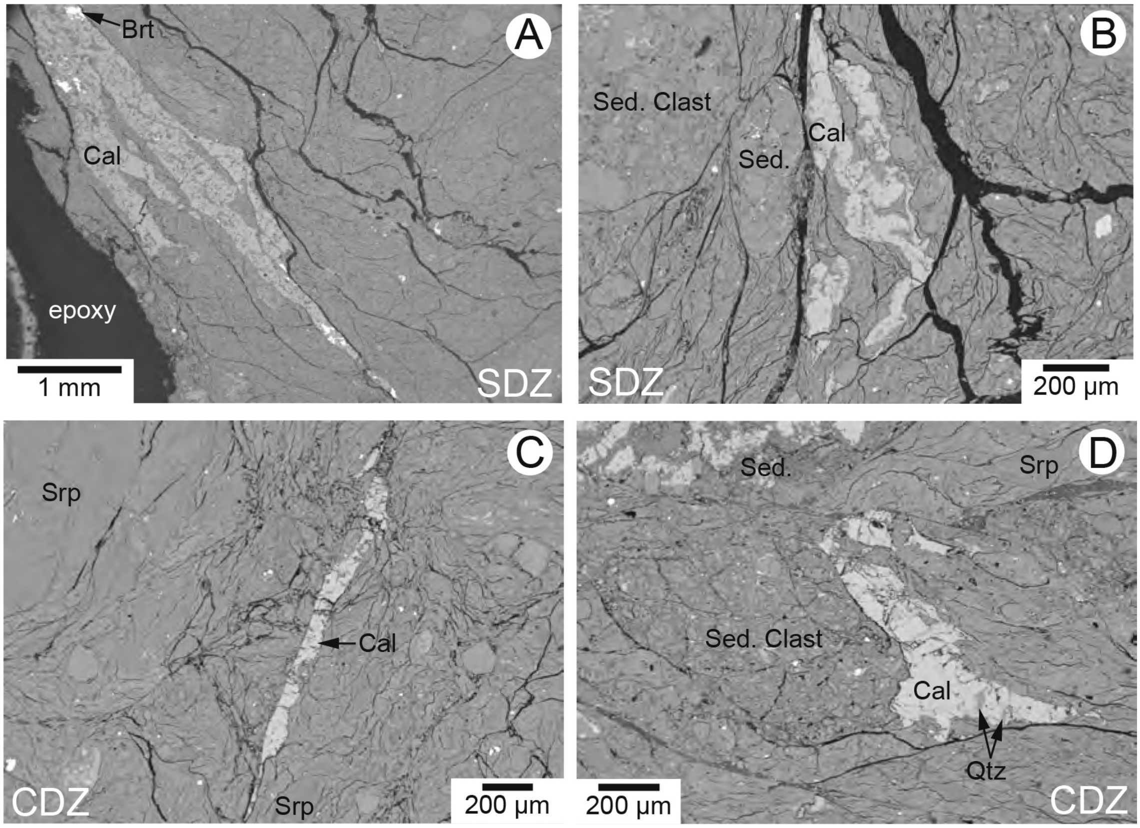

Fig. 8. Calcite veinlets and strain fringes in the clay-rich matrix of the SDZ and CDZ (BSE images). A) Relatively extensive vein of calcite and minor barite (Brt) along folia in the matrix of the SDZ near its NE margin (3197.82 m). Note the relatively straight trend of the main veinlet, which reaches ~6 mm total length, suggestive of recent deposition in the gouge. B) Contorted bands of calcite in clay-rich gouge matrix of the SDZ (3197.71 m); this may represent a somewhat older vein that is being deformed by shear in the gouge matrix. C) Relatively straight band of calcite, ~1.7 mm in length, that is intergrown with some gouge clays in the porphyroclast-rich portion of the CDZ (3298.92 m). The calcite has a blocky character, and it is reasonably free of twins. D) A strain fringe of calcite and minor quartz at the tip of a sedimentary porphyroclast in the CDZ near its NE margin (3298.89 m).

Fig. 9H) (Supplementary Table 4). XRD analyses indicated the presence of both saponite and corrensite in all of the SDZ gouge samples, and the clay compositions and cation ratios in the samples at 3196.38 and 3197.70 m (Fig. 9F and G) are essentially identical to those from the NE-CDZ (Fig. 9E). The samples located near the NE boundary of the SDZ show a slightly wider compositional range along the same linear trend, to Mg/(Mg + Fe) = 0.78 and Si/(Si + Al) = 0.70. Silica contents are as low as ~36 wt% SiO_2 and Al contents as high as 13 wt% Al_2O_3 (Supplementary Table 4). As was also observed in the CDZ, SDZ clays whose compositions correspond to saponite (Fig. 9A) commonly are associated with calcite deposits (Fig. 8A and B) or line fractures in porphyroclasts.

5.3. Altered detrital serpentine clasts in siltstone

Compositions of altered detrital serpentine grains from 2 samples of banded siltstone are plotted in Fig. 10A, and the data are presented in Supplementary Table 5. The Mg/(Mg + Fe) ratio is slightly lower for the clays from the sample with the smaller detrital serpentine component (~2.5% at 3295.26 m compared to ~13% at 3295.53 m; Supplementary Fig. 2). In contrast, the range of Si/(Si + Al) is essentially the same for the analyses from both samples, at 0.65–0.70. The range of Al contents of these minerals is 13.5–15.7 wt% Al_2O_3, whereas the most aluminous SDZ clay contains 13.0 wt% Al_2O_3.

5.4. Chlorite

Chlorite associated with serpentine in the foliated gouges was analyzed for comparison with the clay-mineral compositions. These chlorites form part of the talc + actinolite + chlorite alteration assemblage that is found in some of the serpentinite porphyroclasts (e.g., Fig. 4C and D of Moore and Rymer, 2012), and all three chlorite compositions (Supplementary Table 6) plotted in Fig. 10B are from actinolite ± serpentine-bearing porphyroclasts. The chlorites are relatively fresh, with <0.3 wt% ($CaO + Na_2O + K_2O$), and they have the highest Al (15–20 wt% Al_2O_3) and lowest Si (30.5–32.0 wt% SiO_2) contents of any of the Mg-rich phyllosilicates analyzed in this study. The ratio Si/(Si + Al) of two analyses averages 0.65, whereas that of the third is 0.57. The chlorites are very Mg-rich, with 29–31 wt% MgO; the Mg/(Mg + Fe) ratio of 0.90–0.93 is within the range found for the serpentine minerals.

6. Discussion

6.1. Foliated gouge–wall rock relationships

This study adds to the evidence of the major disconnect between the two creeping traces and the adjoining wall rocks. Laboratory friction data show an abrupt change in coefficient of friction across the boundaries of the CDZ and SDZ with the quartzofeldspathic wall rocks (Lockner et al., 2011; Carpenter et al., 2012). Drilling mud was preferentially injected into the core at the transition from stronger to weaker rocks (Figs. 2 and 3). Recent deformation in the wall rocks at the contacts appears to be restricted to narrow zones of fracturing that overprint older deformation features (Figs. 2–4). The most highly deformed quartzofeldspathic rocks encountered in the Phase 3 core are older fault rocks (Sills,

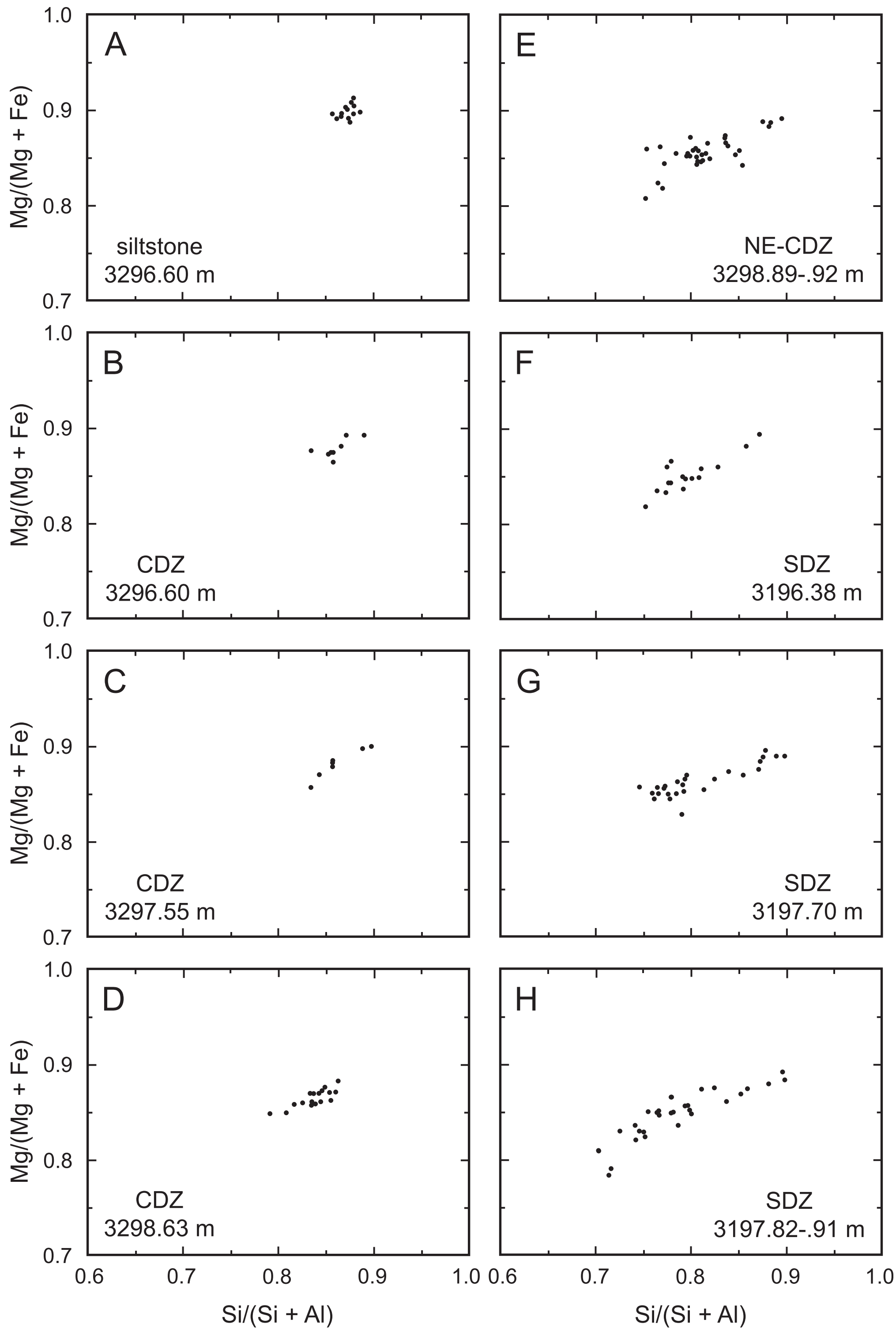

Fig. 9. Comparison of Mg-clay chemistry from the CDZ, SDZ, and adjoining rocks, plotting the atomic ratios Mg/(Mg + Fe) and Si/(Si + Al), where Al is the total Al content. A) Saponite crystallized in veins and patches in the banded siltstone at the contact with the CDZ (3296.60 m); B) SW margin of the CDZ, 3296.60 m; C) CDZ, 3297.55 m; D) CDZ, 3298.63 m; E) the porphyroclast-rich zone at the NE margin of the CDZ (3298.89–3298.92 m); F) SW margin of the SDZ, 3196.38 m; G) the center of the SDZ, 3197.70 m, and H) near the NE boundary, 3197.82–3197.91 m.

2010; Bradbury et al., 2011; Holdsworth et al., 2011) whose location on the SW side of the SDZ is outside the present-day damage zone (Zoback et al., 2010).

Element scans (Figs. 3B and 4B) demonstrate that major differences in rock chemistry between the creeping traces and the surrounding rocks extend to the contacts. Chemical contrasts indicate the presence of marked chemical potential gradients between the ultramafic-rich gouges and the wall rocks that drive metasomatic exchange across the boundaries. The transfer of Mg from the CDZ and SDZ into the surrounding rocks is clearly

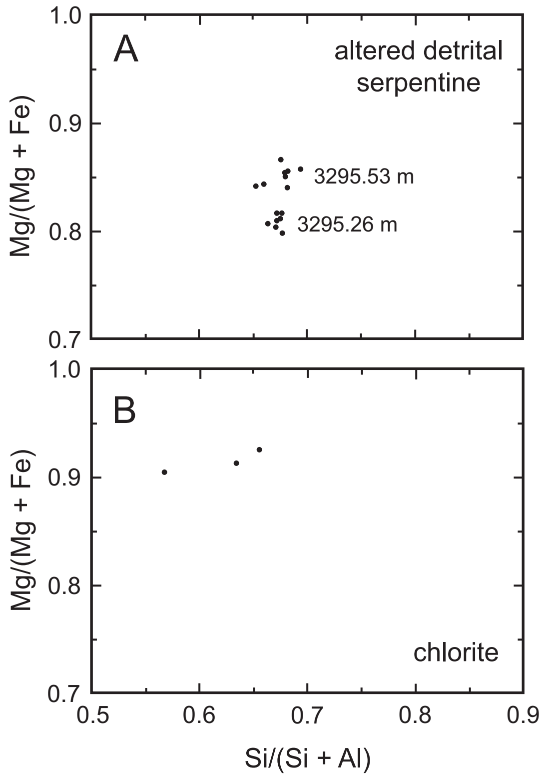

Fig. 10. Atomic ratios Si/(Si + Al) versus Mg/(Mg + Fe) for A) altered detrital serpentine grains from the sanded siltstone, 3295.26 and 3295.53 m and B) chlorite from actinolite ± serpentine-bearing porphyroclasts in the SDZ, 3197.70 m.

discernible in thin section, and was accomplished either through migration of Mg-bearing fluids or the diffusion of Mg ions through a static pore fluid (e.g., Frantz and Mao, 1976, 1979). The migration of Mg-bearing fluids would be a local manifestation of the process postulated by Holdsworth et al. (2011). Much of the Mg is removed from the pore fluids within a few centimeters of the contacts through precipitation of saponite in microfractures. More detailed chemical investigations are needed to fully characterize the extent of chemical exchange across the boundaries. Chemical exchanges involved in the alteration of serpentinite and sedimentary porphyroclasts in the CDZ and SDZ (Bradbury et al., 2011; Hadizadeh et al., 2012; Moore and Rymer, 2012) can serve as a guide for such studies. Crystallization of saponite in the sedimentary porphyroclasts requires an influx of Mg derived from the serpentinite porphyroclasts; in turn, alteration of feldspar in the sedimentary porphyroclasts contributes Al and (Ca + Na + K) to the serpentinite porphyroclasts for saponite growth.

6.2. Controls on mineral occurrence and chemistry

This study has documented a number of differences in the distribution and compositions of the Mg-rich clay minerals encountered in the SAFOD drillhole. Saponite dominates the mineralogy of the CDZ, with the occurrence of corrensite confined to the NE margin (Fig. 6, Supplementary Fig. 4). Indeed, the saponite compositions reported in this study and by Moore and Rymer (2007, 2012) approximate the CDZ whole-rock chemistry (Bradbury et al., 2011), including minor elements such as Ni. Saponite of uniform chemistry also has crystallized in the wall rocks within millimeters of the CDZ on the SW side. Magnesium-rich clays fill fractures in similar occurrences at the other boundaries, as well. Both corrensite and saponite occur throughout the SDZ (Fig. 6, Supplementary Fig. 5).

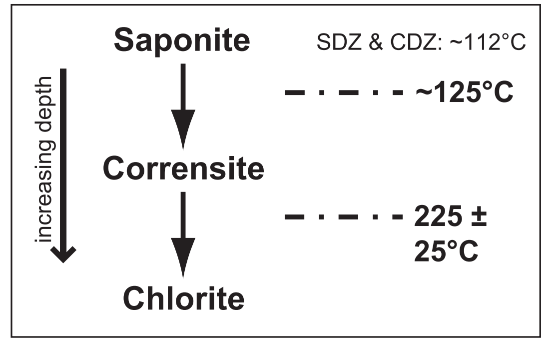

Fig. 11. Estimated stability ranges of Mg-phyllosilicates, based on the thermal stability range of corrensite in the volcanic section of the Coast Range ophiolite determined by Evarts and Schiffman (1983) and Bettison and Schiffman (1988).

The Mg-clay compositions follow a more or less continuous linear trend, and clay compositions from the SDZ and CDZ overlap substantially (Fig. 9). In contrast, phyllosilicates that replaced detrital serpentine grains in the siltstone define a separate, restricted compositional field at lower Si/(Si + Al) ratios than the gouge clays (Fig. 10A). Chlorite also plots separately from the other minerals (Fig. 10B); it lacks a significant clay component and can be considered as a relict, sub-greenschist to greenschist facies metamorphic mineral. From Fig. 9, corrensite has Si/(Si + Al) < 0.80 and the analyses labeled corrensite in Table 2 are from that low-Si group. The corrensite crystal structure is a 50:50 ordered mixture of saponite and chlorite, and averaging the "end-member" saponite (Fig. 9A) and chlorite (Fig. 10B) compositions yields Si/(Si + Al) ~0.75.

A progression from saponite to corrensite to chlorite with increasing depth (i.e., increasing temperature) has been well documented in burial depositional environments and hydrothermal systems, and the mineral sequence represents prograde diagenetic/metamorphic reactions (e.g., Reynolds, 1988). This progressive change in mineralogy is accompanied by decreasing Si and increasing Al contents; consequently, variations in these two elements are largely controlled by temperature. Nevertheless, rock chemistry may exert at least some influence on Si and Al concentrations (Shau and Peacor, 1992). The clay compositions reported in this study are shifted to relatively low Al (high Si/(Si + Al)) contents compared to the same minerals in other occurrences (e.g., Inoue and Utada, 1991; Schiffman and Staudigel, 1995). This may reflect the large ultramafic component of the CDZ and SDZ. The least altered serpentine minerals contain 1–2 wt% Al_2O_3 (Table 2, Supplementary Table 1).

In contrast, the magnesium-to-iron ratio of these phyllosilicate minerals is controlled largely by the bulk rock chemistry (e.g., Bettison-Varga et al., 1991; Bevins et al., 1991; Inoue and Utada, 1991; Schiffman and Fridleiffson, 1991). Except for two analyses from the northeast side of the SDZ, the Mg/(Mg + Fe) ratio of the matrix clays in both creeping traces exceeds 0.80 and in most cases is in the 0.86–0.96 range that characterizes the serpentine minerals. The differences in Mg ratio among the clays replacing detrital serpentine grains correspond to their relative abundance in the siltstone; the minerals with the higher Mg ratios are from the sample with the larger detrital serpentinite contents. Temperature does have some influence on the Mg-to-Fe ratio, however, and a modest reduction in Mg/(Mg + Fe) with the progressive change from saponite to corrensite to chlorite has been reported (e.g., Shau et al., 1990; Schiffman and Staudigel, 1995). Consistent with this, the range of Mg/(Mg + Fe) ratios extends to lower values in the corrensite-bearing SDZ and NE-CDZ samples than in the CDZ samples lacking corrensite (Fig. 9). The high Mg content of chlorite

(Fig. 10B) may reflect the preferential partitioning of Fe into coexisting actinolite.

The temperature ranges over which saponite, corrensite, and chlorite are stable can vary markedly with the geologic setting, e.g., geothermal systems versus burial metamorphism (Reynolds, 1988). The thermal regime at SAFOD corresponds to burial metamorphism, and for this discussion shearing is assumed to enhance reaction rates by lowering kinetic barriers (Vrolijk and van der Pluijm, 1999) but not to modify mineral stabilities. The first appearance of corrensite in burial diagenetic environments can occur at temperatures as low as 60–80 °C (e.g., Reynolds, 1988). Inoue and Utada (1991) studied the smectite-to-chlorite transition in a contact metamorphic sequence in volcaniclastic rocks, concluding that corrensite formed in the T range 100–200 °C. Corrensite was the only Mg-phyllosilicate produced near the lower-T end of this range, whereas corrensite and chlorite occurred together near the high-T end. Evarts and Schiffman (1983) estimated a lower limit of 125 °C and they and Bettison and Schiffman (1988) estimated an upper limit of ~225 °C for corrensite stability at different localities in the Coast Range ophiolite of California. The corrensite in the two ophiolite occurrences formed during hydrothermal alteration of the crustal volcanic section. The lower T limit of the assemblage chlorite + actinolite + talc in metasomatic zones developed between ultramafic and crustal rocks has been estimated to occur at temperatures as low as 225–250 °C (Moore, 1984; Soda and Takagi, 2010).

The chemistry of the chromian spinels in the serpentinite associated with SAFOD indicates a source in the Coast Range ophiolite (Moore and Rymer, 2012), and the range for corrensite stability between 125 and 225 °C estimated for the other two ophiolite occurrences (Evarts and Schiffman, 1983; Bettison and Schiffman, 1988) may also be reasonable for the SAFOD clays (Fig. 11). The lower-T limit is consistent with the evidence that saponite is the stable Mg-rich clay mineral at the depth of Hole G core recovery (~112 °C). The high-temperature limit for corrensite cannot be verified from the SAFOD samples; however, as described above, a range of 225 ± 25 °C for the corrensite-to-chlorite transition is consistent with a number of other natural occurrences. Schleicher et al. (2009, 2012) also suggested that the upper thermal limit for corrensite stability at SAFOD is at or slightly above 200 °C.

6.3. Implications for the SAF at SAFOD

6.3.1. Multiple stages of phyllosilicate growth in the banded siltstone

The chemistry of the clays that pseudomorphically replaced detrital serpentinite grains in the banded siltstone may represent mixtures or interlayers of corrensite and chlorite, akin to those imaged by Schleicher et al. (2012, their Fig. 6). The presence of corrensite + chlorite also is consistent with the XRD data (Fig. 6A), and it would place the crystallization temperature near the upper limit of corrensite stability (Fig. 11), perhaps ~200 °C. Such temperatures would represent ~5–5.5 km depth for a 35°/km geothermal gradient, nearly twice the present depth of the sampled rock unit. The estimated burial depth would increase if the geothermal gradient at the time of crystallization were smaller (see discussion of heat flow in the Coast Ranges by Page et al., 1998).

The spot core recovered from the bottom of the main SAFOD drillhole (3990 m MD, ~3 km vertical depth) consists of fossiliferous siltstones and shales that were identified as Late Cretaceous Great Valley Group rocks (Zoback et al., 2010). The spot core is located well outside the damage zone of the present SAF, whose NE limit is at ~3400 m MD in the main hole. Based on TEM and XRD analyses, Schleicher et al. (2009) identified chlorite + corrensite in these Phase 2 rocks, along with illite-rich authigenic I–S clays that indicated a crystallization temperature of ~200 °C. The detrital composition and fossiliferous character of the siltstone-shales from Hole G Runs 4–6 (Fig. 1) are very similar to those of the spot core. The results of this study further suggest that the banded siltstone in the damage zone shares the same early burial history as the nearby Great Valley Group country rocks.

The crystallization of mixed corrensite + chlorite in the Great Valley rocks may represent diagenetic reactions in the forearc basin. The subsequent partial unroofing of the rock units is likely associated with the uplift of the Diablo Range on the NE side of the SAF creeping section. Page et al. (1998) identified a major episode of uplift and erosion throughout the central and southern Coast Ranges, including the Diablo Range, in response to the change in plate motion to its present oblique convergence. The timing of the change was estimated at ~3.5 Ma by Page et al. (1998), whereas Atwater and Stock (1998) place it at 8 Ma.

6.3.2. Influence of shearing rate variations on the CDZ and SDZ

Based on the deformation of the casing in the main hole, the CDZ takes up most of the fault slip at SAFOD. The CDZ is ~60% wider than the SDZ, and shear distributed uniformly across both zones could account for some of the additional slip of the CDZ. However, the differences in texture and mineral chemistry documented in this study between the SDZ and most of the CDZ also indicate differences in their shearing rates. In addition, the shearing rate is not uniform across the width of the CDZ.

The creeping traces were considered by Moore and Rymer (2012) to have formed as a result of shearing-enhanced reaction of serpentinite with quartzofeldspathic rocks. The good preservation of the serpentinite in outcrop is attributable to low reaction rates at surficial conditions (Moore and Rymer, 2012). Shear at higher temperature, confining pressure, and fluid pressure conditions has led to substantially greater degrees of reaction progress in both the CDZ and SDZ cores. Because the CDZ and SDZ core samples come from nearly the same depth, the higher proportion of Mg-clay-rich matrix and the smaller porphyroclast sizes across most of the CDZ may best be explained by enhanced reaction at a higher shearing rate than is characteristic of the SDZ. The concentration of relatively large porphyroclasts in the NE-CDZ suggests reduced shearing rates near the NE margin. The restricted occurrence of the calcite deposits to the SDZ and NE-CDZ can be explained in the same way as the porphyroclast abundances. The higher shearing rate of much of the CDZ either inhibits the deposition of calcite or, if some deposition occurs, promotes its rapid fragmentation and subsequent dispersal in the gouge.

The distributions of saponite and corrensite and the variations in Mg-clay chemistry in the foliated gouges can also be explained by differences in shearing rate, but such an explanation would require the added factor of a minor decrease in temperature over time. At one time, both the CDZ and SDZ core samples were at temperatures within the corrensite stability range. With declining temperatures to values below ~125 °C (Fig. 11), saponite became the stable phyllosilicate mineral, and newly crystallized clays had compositions similar to those in Fig. 9A. At the same time, pre-existing corrensite began to convert to saponite by some process of fluid-assisted, shearing-promoted recrystallization. Across most of the CDZ, this replacement seems to have progressed sufficiently to destroy the 1:1 ordering of chlorite and saponite layers that defines the corrensite superstructure. Enough chlorite interlayers remain, however, to produce a continuous spread of mixed-layer compositions. Some corrensite is preserved in the more slowly shearing SDZ and NE-CDZ.

The postulated decrease in temperature responsible for the change from corrensite to saponite stability could be achieved in a variety of ways. One possibility is gradually upward migration of the weak gouge materials relative to the wall rocks, either in response to fault-normal compression or as a result of the continued introduction of serpentinite into the fault at depth (Moore and Rymer, 2012). Another possibility is a relatively recent stage of regional uplift and erosion. The transition from saponite to corrensite stability could occur at depths as little as 0.5 km greater than those of core recovery (Fig. 11). The present-day central and southern Coast Ranges are the products of a pulse of folding and thrusting at 0.45–0.40 Ma followed by uplift beginning ~0.4 Ma (Page et al., 1998). Uplift rates in the Diablo Range over this time span were estimated by Page et al. (1998) at 1.4–2.0 mm/yr, based on stratigraphic and structural relations. The amount of uplift at even the lower rate would be sufficient, if matched by erosion along the fault.

The origin of the differences in shearing rate between the CDZ and SDZ and across the CDZ is not known, and it may differ for the two cases. Fault geometry may have played a role. A difference in the orientations of the CDZ and SDZ may have favored shear within the CDZ. In the same way, a geometric irregularity along the NE boundary of the CDZ may have shielded that portion of the creeping trace from some of the shear. Slight initial differences in shearing rate could become augmented over time, as shearing-enhanced reaction weakening further localizes shear in a feedback process. Availability of fluids is critical to most, if not all, of the reaction and deformation processes in the CDZ and SDZ. Thus, differences in permeability or the presence of permeability barriers potentially may also play an important role. The presence of the calcite veins and strain fringes in the clayey matrix of the SDZ and NE-CDZ samples (Fig. 8) would suggest, however, that the availability of fluids was not limited in those areas.

The well-casing deformation associated with the SDZ in the main hole (Zoback et al., 2010, 2011) indicates the continued activity of the SDZ. Although the widths of the CDZ and its associated casing deformation are essentially the same (Zoback et al., 2010, 2011), the possibility nevertheless exists that the narrow NE-CDZ is no longer actively deforming. The nature of the transition between the main part of the CDZ and the NE-CDZ would be informative, a gradual transition suggesting a gradient in creep rate and an abrupt change perhaps signaling the contact between creeping and non-creeping sections. Unfortunately, the gap in core recovery in the area of the transition (Supplementary Fig. 3) may preclude this determination. The absence of calcite veins that crosscut the foliation in the NE-CDZ, however, may indicate some amount of present-day shear.

Whatever the exact causes, the mineralogical and textural differences that have developed between and across the CDZ and SDZ highlight their sensitivity to the conditions of faulting. More detailed investigations of deformation and reaction mechanisms, combined with geochemical and geophysical measurements, should significantly advance our understanding of the development of the creeping traces at SAFOD.

7. Conclusions

The key points of this study are:

(1) Samples that straddle the boundaries of the CDZ and SDZ with the wall rocks in the SAFOD core illustrate the abrupt changes in rock chemistry, mineralogy, and deformation styles and intensity that occur at the contacts. Present-day deformation is highly localized to the CDZ and SDZ, and the rocks immediately adjacent to them are characterized by only minor recent fracturing. Some of these fractures are filled with saponitic clays that were deposited by Mg-rich fluids that migrated short distances into the wall rocks from the creeping traces. With the exception of the fracture fillings, the gouge-wall rock boundaries are marked by abrupt changes in Mg and Si concentrations.

(2) Some differences in mineralogy and texture between the CDZ and SDZ and across the width of the CDZ can be explained in terms of differences in shearing rate. Reaction progress is greater in areas of higher shearing rate, evidenced by a higher Mg-clay content and smaller maximum porphyroclast sizes. Calcite deposits, consisting of veinlets and strain fringes around porphyroclasts, are concentrated in areas of slower shear. The stable Mg-rich clay at the cored depths (112 °C) is saponite, inferred to persist to ~125 °C. The presence of the higher-T clay mineral corrensite in areas of slower shear indicates a decrease in temperature over time, perhaps in response to regional uplift and erosion. Preexisting corrensite was more thoroughly replaced by saponite in those portions of the creeping traces subjected to higher shearing rates. Positive feedback between shearing rate and shear-enhanced reaction weakening may have been instrumental in development of the present-day differences.

Acknowledgments

This paper has benefitted from reviews by W.G. Ernst, J. Hadizadeh, P. Schiffman, an anonymous reviewer, and editor T. Takeshita, and discussions about drilling mud with R. Holdsworth. R. Oscarson and L. Hayden provided assistance with the SEM and microprobe work.

Appendix A. Supplementary data

Supplementary data associated with this article can be found in the online version, at http://dx.doi.org/10.1016/j.jsg.2014.09.002.

References

Atwater, T., Stock, J., 1998. Pacific-North America plate tectonics of the Neogene southwestern United States: an update. Int. Geol. Rev. 40, 375–402. http://dx.doi.org/10/1080/00206819809465216.

Bettison, L.A., Schiffman, P., 1988. Compositional and structural variations of phyllosilicates from the Point Sal ophiolite, California. Am. Miner. 73, 62–76.

Bettison-Varga, L.A., MacKinnon, I.D.R., Schiffman, P., 1991. Integrated TEM, XRD, and electron microprobe investigation of mixed-layered chlorite/smectite from the Point Sal ophiolite, California. J. Met. Geol. 9, 697–710.

Bevins, R.E., Robinson, D., Rowbotham, G., 1991. Compositional variations in mafic phyllosilicates from regional low-grade metabasites and their application of the chlorite geothermometer. J. Met. Geol. 9, 711–721.

Bradbury, K.K., Evans, J.P., Chester, J.S., Chester, F.M., Kirschner, D.L., 2011. Lithology and internal structure of the San Andreas fault at depth based on characterization of Phase 3 whole-rock core in the San Andreas Fault Observatory at Depth (SAFOD) borehole. Earth Planet. Sci. Lett. 310, 131–144. http://dx.doi.org/10.1016/j.epsl.2011.07.020.

Bradbury, K.K., Evans, J.P., Shervais, J.W., 2013. Micro-scale composition and texture of fault rocks from SAFOD core: evidence for deformation processes and fluid-rock reactions. Geol. Soc. Am. Abstr. Progr. 45 (7), 749.

Carpenter, B.M., Saffer, D.M., Marone, C., 2012. Frictional properties and sliding stability of the San Andreas fault from deep drill core. Geology 40 (8), 759–762. http://dx.doi.org/10.1130/G33007.1.

Chester, J.S., Chester, F.M., Sills, D.W., Heron, B., Almeida, R.V., Guilmette, R.N., 2010. Structure of the San Andreas fault at SAFOD. Eos Trans. AGU 91(52). Fall Meeting Supplement, Abstract T52B-03.

Evarts, R.C., Schiffman, P., 1983. Submarine hydrothermal metamorphism of the Del Puerto ophiolite, California. Am. J. Sci. 283, 289–340.

Frantz, J.D., Mao, H.K., 1976. Bimetasomatism resulting from intergranular diffusion. I. A theoretical model for monomineralic reaction zone sequences. Am. J. Sci. 276 (7), 817–840.

Frantz, J.D., Mao, H.K., 1979. Bimetasomatism resulting from intergranular diffusion. II. Prediction of multimineralic zone sequences. Am. J. Sci. 279 (3), 302–323.

Hadizadeh, J., Mittempergher, S., Gratier, J.-P., Renard, F., Di Toro, G., Richard, J., Babaie, H., 2012. A microstructural study of fault rocks from the SAFOD: implications for the deformation mechanisms and strength of the creeping segment of the San Andreas Fault. J. Struct. Geol. 42, 246–260. http://dx.doi.org/10.1016/j.jsg.2012.04.011.

Holdsworth, R.E., Van Diggelen, E.W.E., Spiers, C.J., De Bresser, J.H.P., Walker, R.J., Bowen, L.A., 2011. Fault rocks from the SAFOD core samples: implications for weakening at shallow depths along the San Andreas Fault, California. J. Struct. Geol. 33, 132–144. http://dx.doi.org/10.1016/j.jsg.2010.11.010.
Inoue, A., Utada, M., 1991. Smectite-to-chlorite transformation in thermally metamorphosed volcanoclastic rocks in the Kamikita area, northern Honshu, Japan. Am. Miner. 76, 628–640.
Janssen, C., Wirth, R., Wenk, H.-R., Morales, L., Naumann, R., Kienast, M., Song, S.-R., 2014. Faulting processes in active faults — evidences from TCDP and SAFOD drill core samples. J. Struct. Geol. 65, 100–116. http://dx.doi.org/10.1016/j.jsg.2014.04.004.
Kienast, M., Janssen, C., Wirth, R., Rybacki, E., Morales, L., Dresen, G.H., 2012. Microstructural and geochemical observations on gouge samples from the San Andreas Fault Observatory at Depth (SAFOD). Eos Trans. AGU 93. Fall Meeting Supplement, Abstract MR51A-08.
Lockner, D.A., Morrow, C., Moore, D., Hickman, S., 2011. Low strength of deep San Andreas Fault gouge from SAFOD core. Nature 472, 82–85. http://dx.doi.org/10.1038/nature09927.
McPhee, D.K., Jachens, R.C., Wentworth, C.M., 2004. Crustal structure across the San Andreas Fault at the SAFOD site from potential field and geologic studies. Geophys. Res. Lett. 31, L12S03. http://dx.doi.org/10.1029/2003GL019363.
Moore, D.E., 1984. Metamorphic history of a high-grade blueschist exotic block from the Franciscan Complex, California. J. Petrol. 25, 126–150.
Moore, D.E., Lockner, D.A., 2013. Chemical controls on fault behavior: weakening of serpentinite sheared against quartz-bearing rocks and its significance for fault creep in the San Andreas system. J. Geophys. Res. 118, 1–13. http://dx.doi.org/10.1002/jgrb.50140.
Moore, D.E., Rymer, M.J., 2007. Talc-bearing serpentinite and the creeping section of the San Andreas fault. Nature 448, 795–797. http://dx.doi.org/10.1038/nature06064.
Moore, D.E., Rymer, M.J., 2012. Correlation of clayey gouge in a surface exposure of serpentinite in the San Andreas Fault with gouge from the San Andreas Fault Observatory at Depth. J. Struct. Geol. 38, 51–60. http://dx.doi.org/10.1016/l.jsg.2011.11.014.
Moore, D.M., Reynolds Jr., R.C., 1997. X-Ray Diffraction and the Identification and Analysis of Clay Minerals, second ed. Oxford University Press, Inc., New York.
Morrow, C.A., Lockner, D.A., Moore, D.E., Hickman, S., 2014. Deep permeability of the San Andreas Fault Observatory at Depth (SAFOD) core samples. J. Struct. Geol. 64, 99–114. http://dx.doi.org/10.1016/j.jsg.2013.09.009.
Page, B.M., Thompson, G.A., Coleman, R.G., 1998. Late Cenozoic tectonics of the central and southern Coast Ranges of California. Geol. Soc. Am. Bull. 110 (7), 846–876.
Passchier, C.W., Trouw, R.A.J., 2005. Microtectonics, second ed. Springer, New York.
Reynolds Jr., R.C., 1988. Mixed-layer chlorite minerals. In: Bailey, S.W. (Ed.), Hydrous Phyllosilicates (Exclusive of Micas). Rev. Min. 19, 601–629.
Schiffman, P., Fridleiffson, G.O., 1991. The smectite to chlorite transition in drillhole NJ-15m Nesjavellilr geothermal field, Iceland: XRD, BSE, and electron microprobe investigations. J. Met. Geol. 9, 670–696.
Schiffman, P., Staudigel, H., 1995. The smectite to chlorite transition in a fossil seamount hydrothermal system: the Basement Complex of La Palma, Canary Islands. J. Met. Geol. 13, 487–498.
Schleicher, A.M., Warr, L.N., van der Pluijm, B.A., 2009. On the origin of mixed-layered clay minerals from the San Andreas Fault at 2.5–3 km vertical depth (SAFOD drillhole at Parkfield, California). Contr. Miner. Pet. 157, 173–187.
Schleicher, A.M., van der Pluijm, B.A., Warr, L.M., 2012. Chlorite-smectite clay minerals and fault behavior: new evidence from the San Andreas Fault Observatory at Depth (SAFOD) core. Lithosphere 4 (3), 209–220. http://dx.doi.org/10.1130/L158.1.
Shau, Y.-H., Peacor, D.R., 1992. Phyllosilicates in hydrothermally altered basalts from DSDP Hole 504B, leg 83 — a TEM and AEM study. Contr. Miner. Pet. 112, 119–133.
Shau, Y.-H., Peacor, D.R., Essene, E.J., 1990. Corrensite and mixed-layer chlorite/corrensite in metabasalt from northern Taiwan: TESM, AEM, EMPA, XRD, and optical studies. Contr. Miner. Pet. 105, 123–142.
Sills, D.W., 2010. The Fabric of Clasts, Veins and Foliations within the Actively Creeping Zones of the San Andreas Fault at SAFOD: Implications for Deformation Processes. MS thesis. Texas A&M University.
Soda, Y., Takagi, H., 2010. Sequential deformation from serpentinite mylonite to metasomatic rocks along the Sashu Fault, SW Japan. J. Struct. Geol. 32, 792–802. http://dx.doi.org/10.1016/j.jsg.2010.05.003.
Solum, J.G., et al., 2006. Mineralogical characterization of protolith and fault rocks from the SAFOD main hole. Geophys. Res. Lett. 33, L21314. http://dx.doi.org/10.1029/2006GL027285.
Titus, S.J., DeMets, C., Tikoff, B., 2006. Thirty-five-year creep rates for the creeping segment of the San Andreas Fault and the effects of the 2004 Parkfield earthquake: constraints from alignment arrays, continuous global positioning system, and creepmeters. Bull. Seismol. Soc. Am. 96 (4B), S250–S268. http://dx.doi.org/10.1785/0120050811.
Titus, S.J., Dyson, M., DeMets, C., Tikoff, B., Rolandone, F., Bürgmann, R., 2011. Geologic versus geodetic deformation adjacent to the San Andreas fault, central California. Geol. Soc. Am. Bull. 123 (5/6), 794–820. http://dx.doi.org/10.1130/B30150.1.
Vrolijk, P., van der Pluijm, B.A., 1999. Clay gouge. J. Struct. Geol. 21, 1039–1048.
Zoback, M., Hickman, S., Ellsworth, W., 2010. Scientific drilling into the San Andreas fault zone. Eos Trans. AGU 91 (22), 197–199.
Zoback, M., Hickman, S., Ellsworth, W., 2011. Scientific drilling into the San Andreas Fault Zone — an overview of SAFOD's first five years. Sci. Drill. 11, 14–28.